



Article

Exploring the Stability of Fe–Ni Alloy Nanoparticles Exsolved from Double-Layered Perovskites for Dry Reforming of Methane

Alfonso J. Carrillo *  and José Manuel Serra * 

Instituto de Tecnología Química, Universitat Politècnica de València-CSIC, Avda. Los Naranjos s/n, 46022 Valencia, Spain

* Correspondence: alcardel@itq.upv.es (A.J.C.); jmserra@itq.upv.es (J.M.S.)

Abstract: Exsolution is emerging as a promising route for the creation of nanoparticles that remain anchored to the oxide support, imparting remarkable stability in high temperature chemical processes such as dry reforming of methane. This process takes place at temperatures around 850 °C, which causes sintering-related issues in catalysts prepared using conventional impregnation methods, which could be overcome by using exsolution functionalized oxides. In this work, FeNi₃ alloy nanoparticles exsolved from Sr₂Fe_xNi_{1-x}MoO_{6-δ} double-layered perovskites were evaluated as a dry reforming catalyst, paying special attention to structure–activity relationships. Our results indicate that increasing the Ni content favors the nanoparticle dispersion, eventually leading to increased CO₂ and CH₄ conversions. The exsolved nanoparticles presented remarkable nanoparticle size (ca. 30 nm) stability after the 10 h treatment, although the formation of some phase segregations over the course of the reaction caused a minor decrease in the nanoparticle population. Overall, the results presented here serve as materials processing guidelines that could find further potential use in the design of more efficient (electro)catalysts in other fuel production or energy conversion technologies.

Keywords: exsolution; alloy nanoparticle; dry methane reforming; double-layer perovskite



Citation: Carrillo, A.J.; Serra, J.M. Exploring the Stability of Fe–Ni Alloy Nanoparticles Exsolved from Double-Layered Perovskites for Dry Reforming of Methane. *Catalysts* **2021**, *11*, 741. <https://doi.org/10.3390/catal11060741>

Academic Editor: Kalliopi Kousi

Received: 19 May 2021
Accepted: 15 June 2021
Published: 16 June 2021

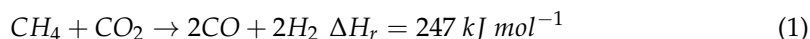
Publisher's Note: MDPI stays neutral with regard to jurisdictional claims in published maps and institutional affiliations.



Copyright: © 2021 by the authors. Licensee MDPI, Basel, Switzerland. This article is an open access article distributed under the terms and conditions of the Creative Commons Attribution (CC BY) license (<https://creativecommons.org/licenses/by/4.0/>).

1. Introduction

A myriad of chemical processes for the production of fuels, pharmaceuticals, fertilizers, or for environmental remediation rely on the use of a metal catalyst dispersed onto oxide supports [1]. These metallic nanoparticles represent the active sites in the heterogeneous reactions and are conventionally deposited on oxide supports (e.g., Al₂O₃, ZrO₂, CeO₂) using impregnation methods. However, in some chemical processes operating at high temperatures, metal nanoparticles created by impregnation can grow due to sintering related processes, resulting in an increase in the particle size and a decrease in the catalyst dispersion [2], which will eventually negatively affect their catalytic activity (Figure 1). This is, for example, the case of the dry reforming of methane (DMR) reaction (Equation (1)).



DMR is a promising technology for the conversion of CH₄ and CO₂ into syngas, which could be further transformed into liquid fuels through Fischer–Tropsch units. However, DMR faces two major issues related to (i) carbon depositions and (ii) metallic nanoparticle sintering, the latter being caused by the elevated process temperatures (600–900 °C) [3].

In order to overcome these challenges, several alternatives have been pursued to obtain more stable metallic catalysts and supports. One method that has attracted attention in the past few years is nanoparticle exsolution due to the high stability that it confers to the metallic catalyst and the strong interaction with the support [2,4–6]. Exsolution consists of the creation of nanoparticles by the migration, under a reductive atmosphere, of cations contained in the bulk of the oxide support that nucleate and grow in the surface. Since the nanoparticles grow from inside, in contrast to the deposited particles, they remain anchored to the oxide surface, which provides high stability against sintering and

coking (Figure 1) [7]. Most works have been focused on nanoparticle exsolution on perovskites [2,4,5], although lately, exsolution has also been observed on other oxides like in fluorite structures [8,9]. Perovskites, of the ABO_3 formula (with $A = \text{La, Sr, Ca, Ba}$, and B , a transition metal cation) have been widely explored as catalysts for DMR based on their high thermal stability [10]. Therefore, it became apparent that exsolution-decorated metallic catalysts based on perovskites could find a remarkable niche of application in DMR [10,11] or other high-temperature thermocatalytic processes such as the chemical looping reforming of methane [12–15]. To our knowledge, the first work devoted to DMR using nanoparticle exsolution was by Zubenko et al., who developed Re–Ni–Fe alloy nanoparticles exsolved from $\text{LaNi}_{0.2}\text{Re}_{0.2}\text{Fe}_{0.6}\text{O}_{3+\delta}\text{-La}_3\text{ReO}_8$ oxide with $x < 0.2$, with ca. 100% CH_4 and CO_2 conversion at 900 °C [16]. One of the additional advantages of exsolution is the ability to create alloy nanoparticles in a facile manner by just adjusting the B-site composition in the perovskite host [16]. As illustrated by Zubenko et al., alloy exsolution can result in high catalytic activity. Other works that have explored bimetallic exsolution for DMR synthesized Fe–Ni, Co–Fe, and Co–Ni alloys exsolved from $(\text{La}_{0.75}\text{Sr}_{0.25})(\text{Cr}_{0.5}\text{Fe}_{0.35}\text{Ni}_{0.15})\text{O}_{3-\delta}$ [17], $\text{Pr}_{0.5}\text{Ba}_{0.5}\text{Mn}_{0.85}\text{Co}_{0.15}\text{O}_{3-\delta}$ (infiltrated with Fe) [18], $\text{Pr}_{0.5}\text{Ba}_{0.5}\text{Mn}_{0.85}\text{Co}_{0.05}\text{Ni}_{0.1}\text{O}_{3-\delta}$ [19], and $\text{La}(\text{Co}_{0.1}\text{Ni}_{0.9})_{0.5}\text{Fe}_{0.5}\text{O}_3$ [20], respectively. The reported CO_2 conversion values using exsolved alloys range from 81% for Fe–Ni [17] to 30% for Co–Fe [18], indicating a better DMR performance of the former. Interestingly, previous reports on bimetallic Fe–Ni catalysts over La_2O_3 showed that this catalyst has no activity to DMR due to encapsulation of Ni by a LaFeO_3 phase [21]. Besides the work of Papargyriou et al., for DMR, several authors have explored Fe–Ni alloy exsolution, especially for solid oxide fuel cells and electrolyzers [22–25]. From these works, it can be noted that the double layer perovskite family $\text{Sr}_2\text{Fe}_{1-x}\text{Mo}_x\text{O}_6$ has been found to have excellent exsolution properties, in which Ni incorporation on the B-site allows for exsolving Fe–Ni alloy nanoparticles after a reduction in H_2 . Despite the promise, these oxides have not been tested for DMR yet. For this reason, in this work, we performed a systematic analysis of the intrinsic (B-site composition) and extrinsic factors (time and temperature) to elucidate their effect on the nanoparticle size and dispersion, and, eventually, the structure–activity relationships in DMR.

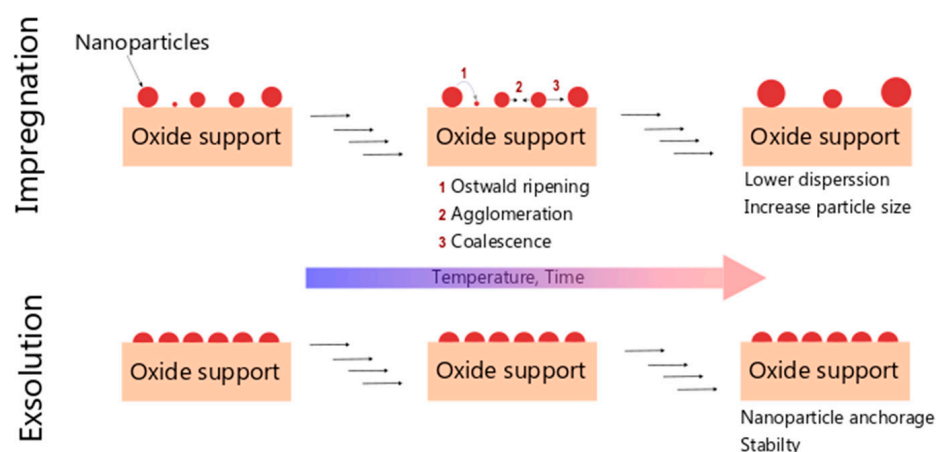


Figure 1. Schematic depicting the morphological evolution differences of dispersed metallic nanoparticles on oxide supports when prepared by impregnation or exsolution methods.

2. Results

2.1. Understanding Fe–Ni Alloy Exsolution on $\text{Sr}_2\text{Fe}_x\text{Ni}_{1-x}\text{MoO}_{6-\delta}$

A series of four samples with $\text{Sr}_2\text{Fe}_x\text{Ni}_{1-x}\text{MoO}_{6-\delta}$ composition ($x = 0.35\text{--}1$, see Table 1) were synthesized via the Pechini method varying the Fe/Ni content. The X-ray patterns depicted in Figure 2a show that all the samples exhibited the tetragonal double-layer perovskite (ICSD 150701, space group, $I4/m$) as the main phase after the calcination treatment at 1100 °C. However, the presence of a secondary impurity phase corresponding to SrMoO_4 was observed for the four samples, in agreement with previous reports in

the literature [26], caused by the high concentration of Mo above the solid solubility [27]. The presence of the impurity decreased with increasing amounts of Ni from 33.4 wt% for SFMO to 9.3 wt% for SFNM35, as analyzed by Rietveld refinement (see example in Figure S1). The increasing presence of Ni stabilized the double-layered perovskite due to its lower oxidation state (+2), which facilitated the presence of Mo in +6 while maintaining charge neutrality. In order to drive the exsolution of metallic nanoparticles, the as-synthesized perovskite powders were treated with a 5% H₂ atmosphere at 900 °C for 2 h. Figure 2b depicts the XRD patterns of the four samples after such treatment. It can be seen that the amount of SrMoO₄ impurities decreased after the treatment in H₂, whereas for SFNM50 and SFNM35, the appearance of minor impurities of a Ruddlesden–Popper-like phase Sr₃MoO₇ was observed. Nevertheless, the double-layered perovskite phase purity increased for the four samples upon hydrogen treatment (Table 1). For instance, SFNM65 purity increased from 83.5 to 86.7%. Importantly, after the 2 h treatment, a negligible phase transition from the double layer perovskite structure to a Ruddlesden–Popper could be ascertained, which was observed previously with other similar compositions (e.g., Sr₂Fe_{1.35}Mo_{0.45}Co_{0.2}O_{6-δ}) [28]. The differences between both works might arise from the different concentration of Fe and Mo on the B-site. In order to provide more insights on the crystallographic changes that occur upon exsolution, we conducted an in situ XRD analysis by heating the SFNM50 sample up to 800 °C under a 5% H₂ atmosphere. Figure 2c shows the evolution of the (1 1 2) reflection located at ca. 32° (room temperature). Upon heating in the H₂ reductive atmosphere, the main reflection gradually shifted toward lower 2θ values. This behavior can be ascribed to the lattice expansion originated by the formation of oxygen vacancies upon reduction and confirms the rise in cell volume as determined from the ex-situ XRD analyses (Table 1). Unfortunately, we were not able to detect the appearance of metal nanoparticles with the current setup, although, as it will be discussed later, these conditions led to metallic nanoparticle exsolution (Figure 3). Figure 2d collects the temperature evolution of the cell volume and lattice parameters as determined by Rietveld refinement. Cell volume for SFNM50 increased from ca. 244 Å³ at 100 °C to ca. 251 Å³ at 800 °C. Both *a*- and *c*-axes from the tetragonal double-layer perovskite lattice elongated upon heating up in the H₂ atmosphere.

Now we turn to the morphological analyses of the materials after the exsolution treatment. Figure 3 depicts the SEM images of the four Sr₂Fe_xNi_{1-x}MoO_{6-δ} samples after 2 h exposure to a 5% H₂ atmosphere at 900 °C. As observed in the SEM images, all the samples exhibited the presence of well-dispersed nanoparticles covering the surface of the porous perovskite except for the sample without Ni, SFMO. Based on this fact, it seems that the presence of Ni on the B-site boosts the metallic nanoparticle exsolution. In the literature, there is a certain discrepancy about the possible exsolution of Fe from SFMO materials. On one hand, Lv and coauthors stated that Sr₂Fe_{1.5}MoO_{6-δ} was stable under reductive environments at high temperatures without evidence of metallic Fe nanoparticle exsolution [28]. They obtained the segregation energy of Fe through DFT calculations, which was 0.91 eV, whereas that of Co was −0.64 eV. These results show that Co exsolution is more thermodynamically favored with respect to Fe in SFMO-like double-layered perovskites. On the other hand, Chen et al. obtained a metallic Fe exsolution from Sr₂Fe_{1.5+x}Mo_{0.5}O_{6-δ} (x = 0–0.1) [29]. In that work, the authors increased the concentration of Fe on the B-site to promote the exsolution of Fe nanoparticles of about 95 nm after 3 h exsolution at 850 °C. Thus, it seems that without Fe excess, as was the case of the present work, Fe exsolution will unlikely happen due to thermodynamic unfavorability, which can be altered by compositional modifications. In the case of the three samples with the presence of Ni on the B-site, nanoparticle exsolution was observed on the surface of the oxide. The nanoparticles were well dispersed over the double-layered perovskite, without evidence of preferential location for the exsolution. Regarding the size, most of the nanoparticles presented diameters in the 20–50 nm range. A more thorough analysis of the nanoparticle size and distribution, and its dependence with exsolution conditions will be covered in the following sections.

Table 1. Label, formula, and crystallographic data of the four $\text{Sr}_2\text{Fe}_x\text{Ni}_{1-x}\text{MoO}_{6-\delta}$ samples before and after exsolution.

Label	Formula	As Prepared			After Exsolution 2 h, 900 °C, 5% H ₂		
		Crystal Phase (Space Group)	Cell Vol. (Å ³)	Phase Purity %	Crystal Phase (Space Group)	Cell Vol. (Å ³)	Phase Purity %
SFMO	$\text{Sr}_2\text{FeMoO}_{6-\delta}$	Tetragonal (I4/m)	244.2	66.6	Tetragonal (I4/m)	244.9	69.1
SFNM65	$\text{Sr}_2\text{Fe}_{0.65}\text{Ni}_{0.35}\text{MoO}_{6-\delta}$	Tetragonal (I4/m)	244.4	83.5	Tetragonal (I4/m)	244.6	86.7
SFNM50	$\text{Sr}_2\text{Fe}_{0.5}\text{Ni}_{0.5}\text{MoO}_{6-\delta}$	Tetragonal (I4/m)	243.9	86.6	Tetragonal (I4/m)	244.4	90.6
SFNM35	$\text{Sr}_2\text{Fe}_{0.35}\text{Ni}_{0.65}\text{MoO}_{6-\delta}$	Tetragonal (I4/m)	243.8	90.7	Tetragonal (I4/m)	244.5	92.2

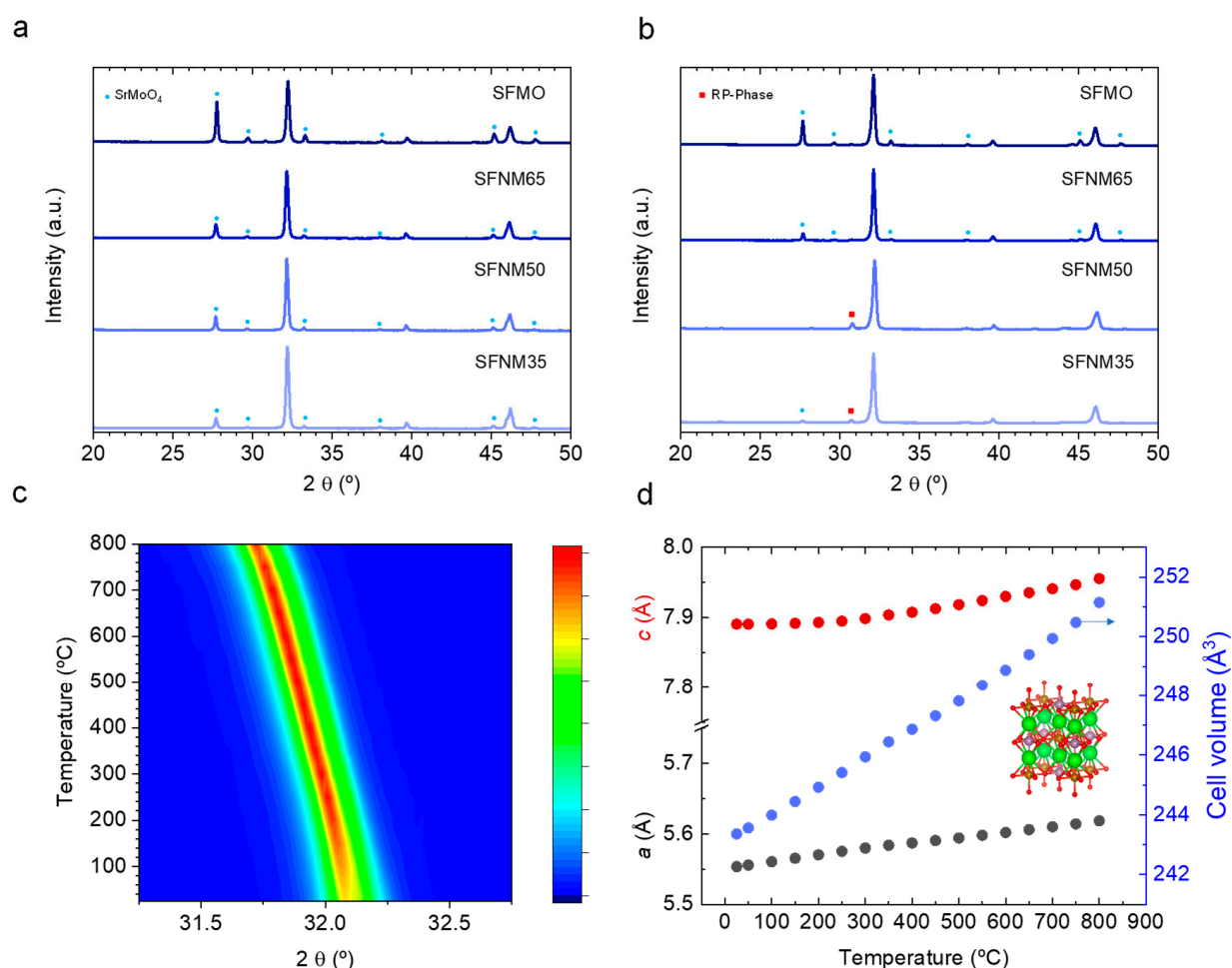


Figure 2. (a) XRD diffractograms of the $\text{Sr}_2\text{Fe}_x\text{Ni}_{1-x}\text{MoO}_{6-\delta}$ materials as-synthesized (calcination at 1100 °C in air). (b) XRD diffractograms of the $\text{Sr}_2\text{Fe}_x\text{Ni}_{1-x}\text{MoO}_{6-\delta}$ materials after the exsolution treatment (5% H₂, 900 °C, 2 h). (c) In situ XRD experiment performed to SFNM50, heating up to 800 °C under 5% H₂. The selected zone depicts the most intense reflection of the tetragonal double layer perovskite. (d) Tetragonal lattice parameters (a, c) and lattice volume variation extracted from the in situ XRD tests for the SFNM50 sample. The schematic inside the figure depicts the tetragonal double layer perovskite crystalline structure (green, red, purple, and brown spheres are Sr, O, Mo, and Fe/Ni atoms, respectively).

Next, we analyzed SFNM65 samples with TEM in order to better understand the nature of the exsolved nanoparticles. Figure 4a shows the HRTEM images of the SFNM65 sample after 2 h exsolution under 5% H₂ at 900 °C. The presence of exsolved nanoparticles of about 20 nm size were observed, which were partly submerged into the perovskite backbone. This characteristic anchoring, typical of nanoparticle exsolution, avoids sintering

with neighboring particles due to the high degree of attachment of the nanoparticles to the oxide surface. Figure 4b–f shows the HAADF-STEM image and EDX mapping of the five elements that compose the double-layer perovskite. These images provide important insights on the composition of the exsolved nanoparticles. As can be seen in the EDX mapping in Figure 4c,d, the nanoparticles were composed of both Ni and Fe, thus the reductive treatment performed in this work resulted in the exsolution of the Ni–Fe alloy nanoparticles from $\text{Sr}_2\text{Fe}_x\text{Ni}_{1-x}\text{MoO}_{6-\delta}$ materials while maintaining the double-layer perovskite structure. As observed in Figure 4c–g, the presence of the initial five elements that composed the perovskite was detected in the backbone, whereas only Fe and Ni were observed in the exsolved nanoparticles. Fe–Ni alloy exsolution has been previously reported in Sr–Fe–Mo based perovskites [22,30–32], titanates [25], and chromites [17,33]. In most of these cases, the composition of the exsolved alloy was FeNi_3 . For instance, in the work of Du et al., they obtained FeNi_3 exsolution from $\text{Sr}_2\text{FeMo}_{0.65}\text{Ni}_{0.35}\text{O}_{6-\delta}$ after 10 h of treatment in pure H_2 [22]. Increased exposure times and higher H_2 concentrations, as performed by Du et al. compared to our work, commonly resulted in larger particle sizes [34,35]. Formation of larger particles could eventually ease their detection by XRD, and, thus the identification of the actual alloy composition of the exsolved nanoparticles. For that reason, we performed a 20 h exsolution treatment at 900 °C in a 5% H_2 atmosphere. Figure 5a depicts a comparison of the XRD patterns for SFNM65 as-synthesized, and after 2 and 20 h exsolution. The exsolution time increase led to several changes in the crystal structure of the SFNM65 material. First, the impurities of SrMoO_4 disappeared. Second, there was a remarkable phase transformation, resulting in the formation of a Ruddlesden–Popper phase $\text{Sr}_3\text{FeMoO}_7$ (ICSD 152243). This result is in line with previous reports by Du et al. (FeNi_3 exsolution from $\text{Sr}_2\text{FeMo}_{0.65}\text{Ni}_{0.35}\text{O}_{6-\delta}$) [22] and Lv et al. (CoFe exsolution on $\text{Sr}_2(\text{Fe}_{1.35}\text{Mo}_{0.45}\text{Co}_{0.2})_{1-z}\text{O}_{6-\delta}$) [28], in which the Ruddlesden–Popper phase appeared after 10 h and 4 h treatment, respectively. Third, the presence of a Fe–Ni alloy with composition FeNi_3 (cubic, ICSD 5116, space group, Pm-3m) was detected, with the main reflections appearing at $2\theta = 44.0$ and 51.3° . For the sake of comparison, the main XRD reflections of Fe and Ni metal are plotted in Figure 5a, which did not correspond to any of the peaks present in the SFNM65 material after 20 h exsolution treatment. The detection of the alloy phase was possible by the larger particle size obtained after using a more prolonged treatment (20 h instead of 2 h). As observed in Figure 5b, the longer exsolution treatment time resulted in larger nanoparticles, with a particle size of 65 nm, although particles as large as 110 nm were also observed, which facilitated the detection of the exsolved alloy phase by XRD. Although the goal of this treatment was to determine the composition of the exsolved alloy nanoparticles, it also provided information about the effects of prolonged exsolution treatment on the particle size, and eventually on the perovskite backbone stability. Here, it is shown that the particle size can be modified by exposing the materials to more prolonged times, however, it results in larger particles, and, especially, in a phase transition of the perovskite backbone, which might have detrimental effects on the catalytic activity. Our results, however, are in contrast with Wang et al., who did not observe particle size enlargement when increasing the treatment time from 3 to 40 h in humidified H_2 at 800 °C using $\text{Sr}_2\text{Fe}_{1.3}\text{Ni}_{0.2}\text{Mo}_{0.5}\text{O}_{6-\delta}$ sintered bars (exsolution of 26 nm Fe–Ni alloys) [23]. Probable causes from the discrepancies of both works can arise from differences in the materials' composition and processing. The use of dense sintered bars could affect the mechanism of nanoparticle growth, since it has been shown that smaller grain sizes could favor the exsolution extent [36].

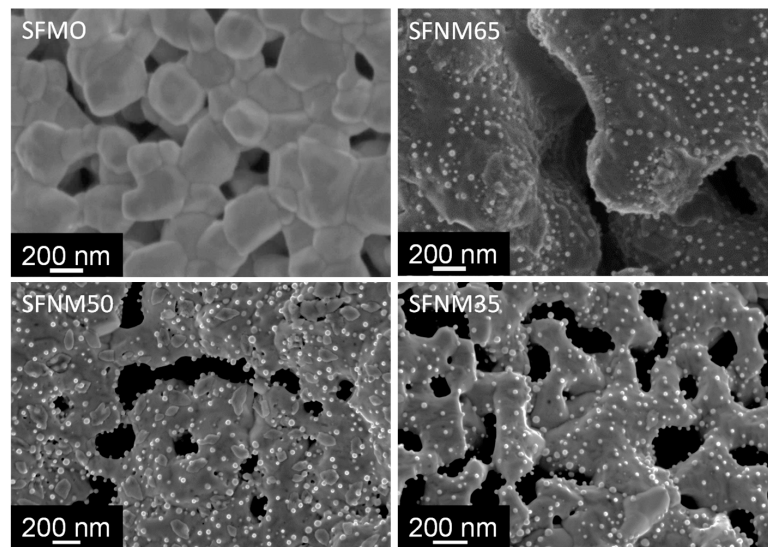


Figure 3. SEM micrographs of the $\text{Sr}_2\text{Fe}_x\text{Ni}_{1-x}\text{MoO}_{6-\delta}$ materials after the exsolution process carried out at 900°C for 2 h under a 5% H_2 atmosphere.

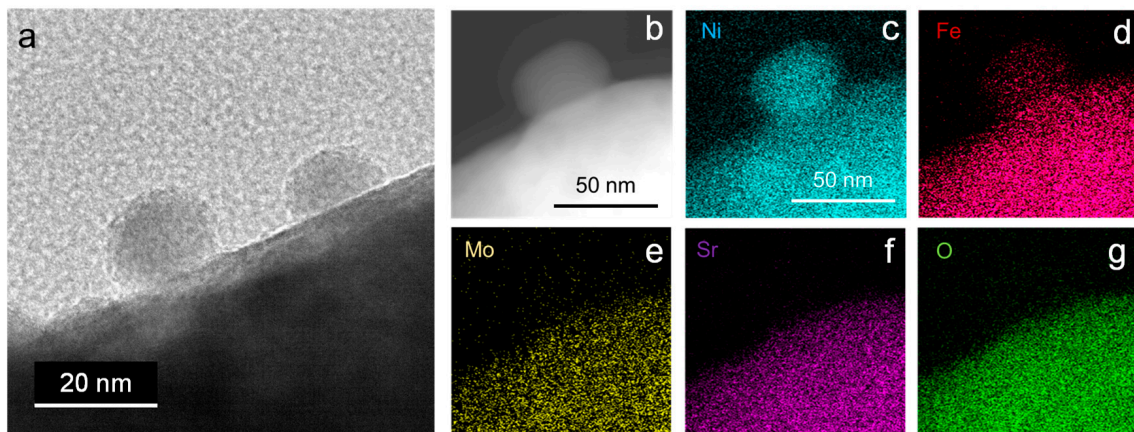


Figure 4. (a) TEM image of the SFNM65 material after 2 h exsolution at 900°C under 5% H_2 , depicting the exsolved nanoparticles. (b) HAADF-STEM image of SFNM65 (c–g) EDX mapping images for Ni, Fe, Mo, Sr, and O, respectively, showing that the exsolved nanoparticles are just composed by Fe and Ni.

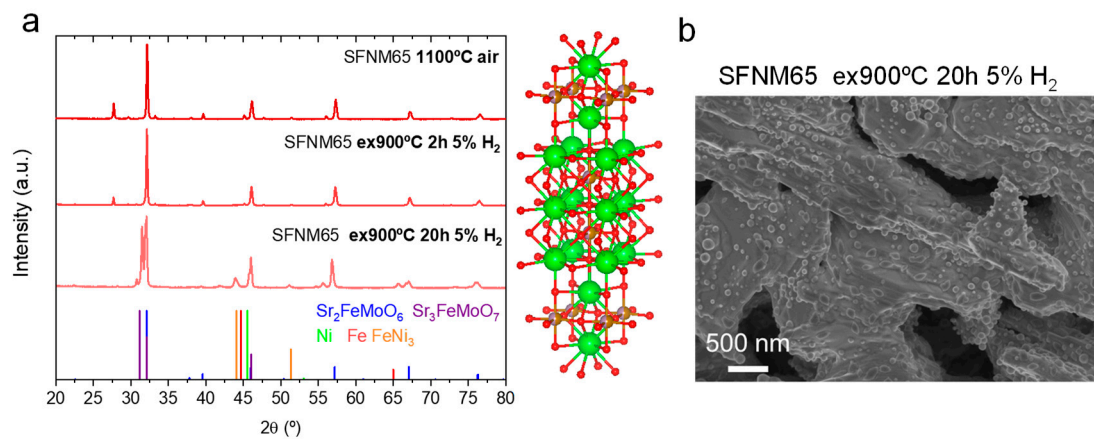


Figure 5. (a) Comparative of the XRD patterns of the SFNM65 material as-synthesized, and after 2 h and 20 h exsolution at 900°C in a 5% H_2 atmosphere. Crystal structure of a $\text{Sr}_3\text{FeMoO}_7$ Ruddlesden–Popper phase. Green, brown, and red spheres represent Sr, Fe/Mo, and oxygen atoms, respectively. Structure drawn with VESTA [37]. (b) SEM image of the SFNM65 material after 20 h exsolution. Fe and Ni reflections are shown in (a) for the sake of comparison.

An alternative way to tune the particle size in exsolution is with temperature [12,34,35,38]. In order to explore this aspect, we treated the double layer perovskite materials at 700 and 800 °C and compared them with the original exsolution temperature, 900 °C. As observed in Figure 6a, there were remarkable differences on the exsolved nanoparticle sizes when lowering the temperature. Namely, the exsolved nanoparticle sizes (d_{50}) were 15.6 ± 4.6 , 24.4 ± 5.4 , and 31.0 ± 8.4 nm at 600, 700, and 900 °C, respectively. The monotonic increase in the particle size with temperature observed in this work was in line with previous reports that indicate, based on the nucleation theory, that increasing the temperature particularly affects the particle growth [12]. It can also be observed that lowering the temperature (700 °C) resulted in a more uniform particle size distribution, whereas at 900 °C, the distribution was much wider (Figure 6b). On the other hand, we did not observe a clear trend when analyzing the effect of temperature in the exsolved particle population (Figure 6c). The treatment at 700 °C resulted in a particle population of $84 \mu\text{m}^{-2}$, which decreased at 800 °C ($59 \mu\text{m}^{-2}$) and reached a maximum value at 900 °C ($88 \mu\text{m}^{-2}$). In other perovskite oxide systems, especially the widely studied Ni exsolution on titanates, the increase in temperature leads to an increase in particle size and a decrease in nanoparticle dispersion [12,34]. Interestingly, in the $\text{Sr}_2\text{Fe}_x\text{Ni}_{1-x}\text{MoO}_{6-\delta}$ system studied here, the standard treatment performed initially (900 °C, 2 h) led to the highest degree of nanoparticle dispersion (also observed in SFNM35 and SFNM65, Figure 3).

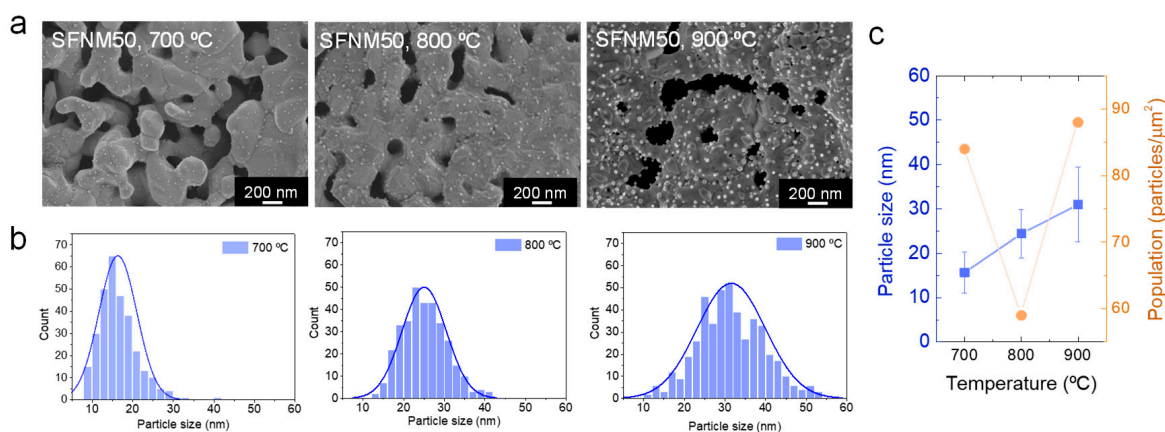


Figure 6. Influence of exsolution temperature on the particle size and population. (a) SEM images of SFNM50 material after exsolution at 700, 800, and 900 °C during 2 h in a 5% H_2 atmosphere. (b) Particle size distribution histograms. (c) Particle size and population versus temperature.

In summary, throughout this section, the effect that extrinsic (temperature, time) and intrinsic (B-site composition) factors have on the nanoparticle exsolution in $\text{Sr}_2\text{Fe}_x\text{Ni}_{1-x}\text{MoO}_{6-\delta}$ double-layer perovskites was studied. We confirmed nanoparticle exsolution of an alloy composition of FeNi_3 . Additionally, in the absence of Ni (i.e., SFMO sample), metallic exsolution was not observed. Increasing exsolution time and temperature led to larger particles, and, in the case of the former, also to a major phase transformation into a Ruddlesden–Popper phase.

2.2. Dry Reforming Tests on Fe–Ni Alloy Exsolved Nanoparticles

In the previous section, we showed that by appropriately selecting the reductive treatment conditions, it is possible to tune the exsolved nanoparticle size and dispersion. Regarding the time, the shortest treatment of 2 h led to the optimum results in terms of particle size and perovskite-backbone stability. In the case of temperature, the smallest particles were obtained at 700 °C (ca. 15 nm), whereas the highest dispersion was observed at 900 °C ($87 \mu\text{m}^{-2}$, $d_{50} \sim 31$ nm). Although materials with smaller nanoparticles will be ideally preferred for the catalysis, the reaction process temperature adds some restrictions to the exsolution temperature. Even if exsolution is known to alleviate particle sintering, it is not advisable to perform nanoparticle exsolution at temperatures lower than the reaction

temperature, since the particles could eventually grow, even if anchored, during the reaction, resulting in variations in the catalytic activity. For the catalytic test, the temperature of choice was 850 °C, since it is the optimal temperature for dry reforming of methane [3]. Due to the endothermic nature of the reaction, lowering the process temperature will decrease the equilibrium conversion [8]. Thus, the materials used for the dry reforming test were treated at 900 °C for 2 h in a 5% H₂ atmosphere in order to drive the exsolution (Figure 3).

The dry reforming catalytic tests were performed in a fixed bed quartz reactor. The exsolution-treated samples were heated in an Ar atmosphere up to 850 °C, the temperature at which the dry reforming reaction was performed for 10 h. The main goals of these catalytic tests were two-fold. First, to evaluate the catalytic activity of the four synthesized samples to ascertain the possible structure–activity relationships derived from the different compositions of the B-site sublattice (i.e., different Fe/Ni ratios). Second, to determine the stability of the exsolved nanoparticles after 10 h under dry reforming conditions at 850 °C. Here, we would like to note that our experiments were carried out with dilute streams of CH₄ and CO₂ to facilitate the screening of our materials. Ideally, pure streams of CH₄ and CO₂ will be used in industrial operation.

Figure 7a,b show the CO₂ and CH₄ conversion (X_{CO_2} and X_{CH_4}) versus time for the four samples, respectively. Regarding the X_{CO_2} , it can be observed that, overall, for the four samples, it was stable during the 10 h test excluding the first injection. From the four samples tested, SFNM50 showed the highest decay in X_{CO_2} going from 72% (second injection) to ca. 70% (10 h). For SFMO and SFM35, the CO₂ conversion slightly increased during the first 2 h of reaction. SFNM35 and SFNM50 showed the highest CO₂ conversion values, which progressively decay with lowering the Ni content. In Figure 7c, the X_{CO_2} after 10 h is shown and plotted versus the Ni content. The X_{CO_2} values with decreasing Ni content in Sr₂Fe_xNi_{1-x}MoO_{6-δ} were 72, 70, 64, and 45% for $x = 0.65, 0.5, 0.35, \text{ and } 0$, respectively. A similar trend was observed for the CH₄ conversion in Figure 7b, although the overall conversion values were lower than for CO₂. After 10 h, the X_{CH_4} values with decreasing Ni content were 47, 43, 37, and 26% for $x = 0.65, 0.5, 0.35, \text{ and } 0$, respectively. In terms of stability, the SFNM50 exhibited a progressive decay on its X_{CH_4} values, which limits its further applicability, which went from 52 to 43% in 10 h on stream. For all the samples tested, CO₂ conversion was higher than CH₄ conversion. This fact resulted in H₂/CO ratios below the stoichiometric value (Figure 7c), which according to Equation (1), should be equal to 1. This is caused by the competing reverse water-gas shift reaction (Equation (2)). Regarding the H₂/CO ratios, the trends are analogous to the CO₂ and CH₄ conversion, being the highest value achieved (H₂/CO = 0.49) for the sample with the highest Ni content, SFNM35 (Figure 7c). H₂ (S_{H_2}) and CO selectivity (S_{CO}) are depicted in Figure S2 (Supplementary Materials). The values, taken at the end of the reaction, show that both parameters increase with increasing Ni content. Namely, SFMO showed ca. 20% selectivity toward CO production, whereas for SFNM35 (the highest Ni content), S_{CO} was around 52%. As expected from the H₂/CO ratios lower than 1, S_{CO} values were higher than S_{H_2} . For instance, H₂ selectivity for SFNM35 was ca. 32%.



To check the stability of the exsolved nanoparticles, the four samples were analyzed by SEM after the 10 h dry reforming reaction test (Figure 8a). It can be observed that the three samples that presented nanoparticle exsolution before the reaction (those with Ni on B-site) also exhibited exsolved nanoparticles after the 10 h of the dry reforming test at 850 °C. Through image analyses of the materials after the reaction, we observed that the particle size values were in the range of the values obtained before the reaction. This result emphasizes the robustness of nanoparticles created by the exsolution method. For instance, the SFNM50 material showed exsolved nanoparticles of ~31 nm before (Figure 6c) and after the reaction (Figure 7c), maintaining the initial values. SFNM35 and SFNM65 presented nanoparticle sizes of ~29 and 26 nm after the reaction, which in both cases were lower than SFNM50. The exsolved nanoparticle dispersion after the reaction is shown in Figure 7c. The observed trend indicates that the amount of exsolved

nanoparticles increased with the Ni content. Namely, the nanoparticle population was 51, 70, and 85 μm^{-2} for SFNM65, SFNM50, and SFNM35, respectively. Interestingly, SFNM50 showed a nanoparticle population of 88 μm^{-2} before the reaction (Figure 6c), which decreased to 70 μm^{-2} after the reaction. This decay on the nanoparticle dispersion correlates well with the decay in the catalytic activity by SFNM50, especially observed for the CH_4 conversion (Figure 7b). In addition, the SFNM50 image after the reaction depicted in Figure 8 revealed the appearance of a major phase segregation that was not observed before the reaction (Figure 3). The formation of this additional phase (characterized by its darker color) could be the responsible for the decay on the nanoparticle population after reaction. As observed in the SEM image (Figure 8), this segregated phase did not exhibit nanoparticle exsolution. XRD was utilized to confirm the nature of this phase. Figure 8b shows the XRD patterns of the four samples after the dry reforming reaction tests. The main impurity corresponds to SrMoO_4 , which was present on the as-synthesized materials (Figure 2a), disappeared after the exsolution treatment (Figure 2b), and regenerated during the 10 h dry reforming test. In addition, we identified the presence of SrCO_3 signatures at $2\theta = 25\text{--}26^\circ$ (Figure 8b) as a consequence of the reaction of Sr^{2+} with the CO_2 used for the dry reforming tests. Carbonation of A-site cations in perovskites (e.g., Sr, Ca, Ba) is known to be a major issue in several CO_2 valorization processes [39,40], although for most of the samples, its presence was negligible. The material that was more affected by Sr carbonation was SFNM50. The concentration of impurity phases after the reaction was determined by Rietveld refinement, indicating a 7.9% of SrCO_3 in SFNM50 material after the reaction. Furthermore, it showed 51.6% of SrMoO_4 , making SFNM50 the sample in which the double perovskite phase, which supports the exsolved nanoparticles, was more degraded after the dry reforming test. This fact had strong implications on the exsolved nanoparticle dispersion, since SrMoO_4 and SrCO_3 were not expected to allocate Ni and/or Fe cations in their crystal lattices, thus, limiting the amount of available surface with the presence of alloy nanoparticles. In particular, the exsolved nanoparticle dispersion of SFNM50 decreased from 88 particles μm^{-2} (Figure 6c) to 70 particles μm^{-2} (Figure 7c). The combination of both facts, the appearance of the SrMoO_4 segregated phase and the decrease in the nanoparticle dispersion, might be responsible for the progressive decay in the SFNM50 CH_4 conversion observed in Figure 7b. In the case of SFNM35, such decay was more attenuated, which could correlate well with a lower amount of detected phase segregation after reaction. Namely, SFNM35 exhibited 3.9% and 44.3% for the SrCO_3 and SrMoO_4 impurity phases, respectively. Interestingly, samples SFMO and SFM65, which exhibited lower CH_4 and CO_2 conversion values, presented minor contributions of the phase segregation after the reaction. For instance, SFMO showed a negligible presence of SrCO_3 (0.1%) and 27.8% of SrMoO_4 , with the latter in the concentration range detected before the reaction (Table 1). Next, we conducted Raman spectroscopy to analyze the possible formation of carbon deposits during the 10 h reaction test. Figure 8c shows the Raman spectra of the four samples after the reaction, depicting the 1000–2500 cm^{-1} wavenumber region, in which modes related to carbon species are expected to appear. Namely, the D and G bands were located at 1368 and 1560 cm^{-1} , respectively [41]. Only a minor contribution of the mode at around 1560 cm^{-1} (ascribed to the G band) was observed for the samples SFNM50 and SFNM65, whereas no modes related to carbon deposition were observed for SFNM35, confirming the high resistance to coking obtained with the exsolution method [7]. With these postmortem analyses, we can conclude that the morphological changes suffered by the materials were mostly related with phase segregations occurring in the host perovskite matrix, whereas the exsolved nanoparticles exhibited high stability, which were responsible for an increase in the catalytic activity. It was observed that a higher Ni/Fe ratio favors a higher population of FeNi_3 nanoparticles, ascribed to the thermodynamically favorability for Ni cations to exsolve over Fe cations, resulting in these Ni rich metallic alloys. Nonetheless, even if the nanoparticles retain its initial particle size and level of anchoring, the presence of phase segregations alter the nanoparticle population if, as was the case here, the segregations do not allocate exsolved nanoparticles. This fact caused a decrease in the CH_4 conversion for

the SFM50 sample (Figure 7b), which is the material that presented the highest presence of phase impurities (SrCO_3 and SrMoO_4) after the reaction (Figure 8b). Eventually, this issue could be tackled by designing perovskite compositions with A-site deficiency and with a higher Fe(Ni)/Mo ratio on the B-site. In this case, A-site deficiency could favor a higher extent of nanoparticle exsolution.

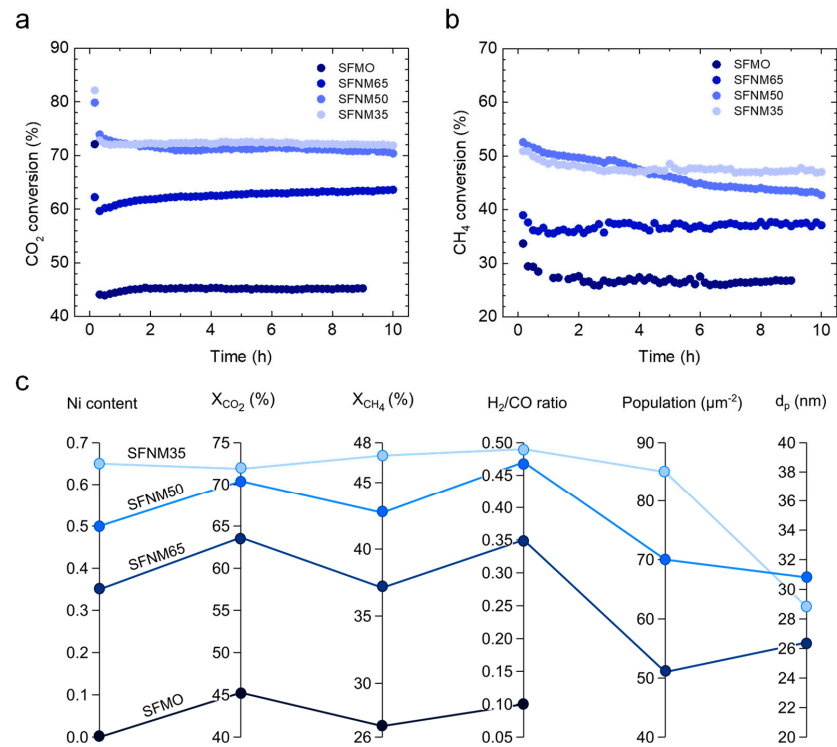


Figure 7. (a) CO₂ (X_{CO_2}) and (b) CH₄ conversion (X_{CH_4}) for the dry reforming reaction tests carried out at 850 °C, during 10 h in a fixed bed quartz tube reactor. CO₂:CH₄:Ar, 5:5:90, SV = 24 L g_{cat}⁻¹ h⁻¹ (c) Composition–structure–performance comparative of Ni content, CO₂, and CH₄ conversion, and H₂/CO ratio at 10 h dry reforming test, nanoparticle population, and exsolved nanoparticle size (d_p).

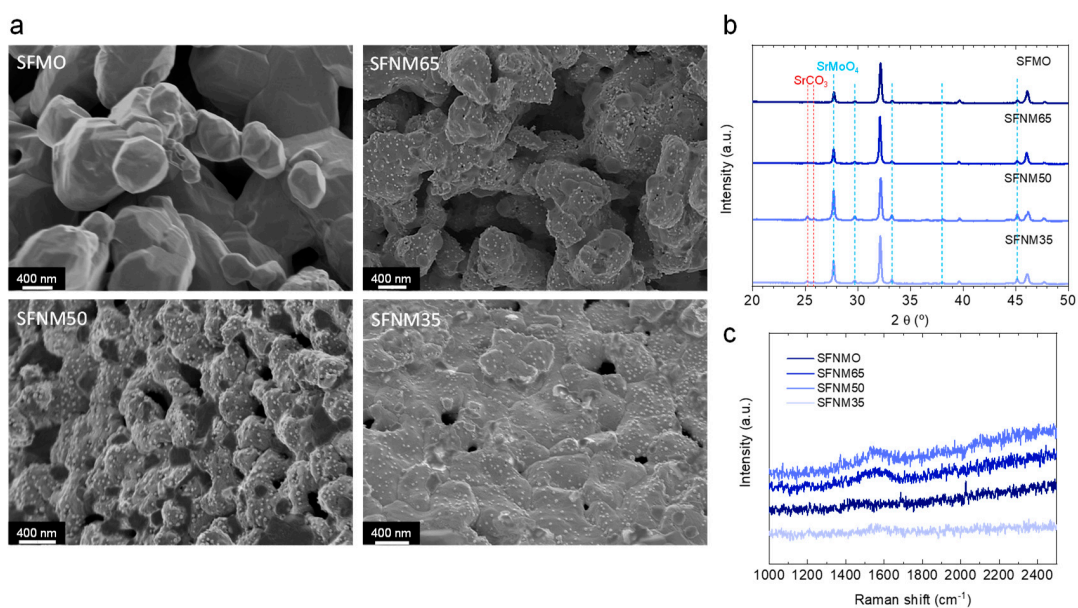


Figure 8. (a) SEM images, (b) XRD patterns, and (c) Raman spectra of the four $\text{Sr}_2\text{Fe}_x\text{Ni}_{1-x}\text{MoO}_{6-\delta}$ samples after the reaction (850 °C, 10 h, 5%vol. CO₂, 5%vol. CH₄, 100 mL min⁻¹ of total flow). Figure (c) depicts the 1000–2500 cm⁻¹ region to show the modes associated with carbon deposition.

3. Conclusions

In this work, we investigated the influence that extrinsic (time, temperature) and intrinsic (B-site composition) factors had on the exsolution of Fe–Ni alloys in $\text{Sr}_2\text{Fe}_x\text{Ni}_{1-x}\text{MoO}_{6-\delta}$ double-layer perovskite materials, and eventually, to its catalytic activity in the dry reforming of methane. Our results indicate that a higher Ni content facilitates the exsolution, illustrated by higher values of nanoparticle population for Ni-rich compositions and the absence of nanoparticle exsolution on the $\text{Sr}_2\text{FeMoO}_6$ sample. These results connect well with literature reports that indicate that Ni has more favorable thermodynamics to exsolve than Fe. This fact might be the reason behind obtaining a Ni-rich alloy composition (FeNi_3) after exsolution, as observed by EDX and XRD. The evaluation of the extrinsic factors pointed to larger nanoparticles with increasing temperature and time, and in the latter case, to a crystallographic phase transition in which a Ruddlesden–Popper phase is predominant. Dry reforming tests indicate that increasing Ni/Fe ratio in the B-site favored both CO_2 and CH_4 conversion, which was ascribed to a higher nanoparticle population obtained with higher Ni content. The nanoparticle size (ca. 30 nm) was remarkably stable after the 10 h dry reforming reaction, corroborating the benefits of exsolution in high temperature thermochemical processes. In addition, Raman spectroscopy illustrated the low tendency to form carbon depositions. However, oxide and carbonate segregations, observed after the catalytic test, caused a decrease in nanoparticle population that especially affected the CH_4 conversion in the Fe/Ni = 1 sample. The results presented here illustrate the potential of double-layered perovskites as host for alloy nanoparticle exsolution and its potential use in high temperature thermocatalytic fuel production. Optimization of the perovskite host to avoid phase segregations via A-site deficiency or B-site doping could eventually increase the nanoparticle dispersion and catalytic activity for the dry reforming of methane or other energy related high temperature chemical processes.

4. Materials and Methods

4.1. Materials Synthesis

$\text{Sr}_2\text{Fe}_x\text{Ni}_{1-x}\text{MoO}_{6-\delta}$ materials with $x = 0.35\text{--}1$ were synthesized through a modified version of the Pechini method. Metal precursors, $\text{Sr}(\text{NO}_3)_2$ (99%, Sigma Aldrich (St. Louis, MO, USA)); $\text{Fe}(\text{NO}_3)_3 \cdot 9\text{H}_2\text{O}$ (98%, Sigma Aldrich); $\text{H}_{24}\text{Mo}_7\text{N}_6\text{O}_{24} \cdot 4\text{H}_2\text{O}$ (98%, Sigma Aldrich); and $\text{Ni}(\text{NO}_3)_2 \cdot 6\text{H}_2\text{O}$ (98%, Sigma Aldrich) were dissolved in deionized water and mixed with citric acid, CA (99%, Sigma Aldrich-Merck) at 60 °C under constant stirring during 3 h, using a metal precursor:CA molar ratio of 1:1.5. Afterward, ethylene glycol, EG, (99%, Sigma Aldrich-Merck) was added to the mixture and the temperature was increased to 80 °C for 2 h, with a CA:EG ratio of 2/3 wt%. After most of the solution was evaporated, it was transferred to a drying oven and heated at 220 °C overnight, a process in which gelification and calcination of the gel took place. Then, the dry powders were ground into fine powders with an agate mortar and calcined at 1100 °C for 10 h to obtain the double-perovskite phase. Nanoparticle exsolution was carried out in a horizontal tubular furnace at 900 °C for 2 h under a 5% H_2 / Ar flow, unless otherwise specified in the text.

4.2. Physicochemical Characterization

X-ray diffractometry (XRD) was performed utilizing a PANalytical CubiX fast diffractometer (Almelo, The Netherlands) using $\text{CuK}\alpha_{1,2}$ radiation and a X'Celerator detector in Bragg–Brentano geometry. XRD patterns were recorded in the 2θ range 20° to 70° and analyzed using the software X'Pert Highscore Plus (Almelo, The Netherlands). In-situ XRD tests were carried out in an Anton Paar XRK-900 reaction chamber attached to the diffractometer. Raman spectroscopy was performed with a Renishaw Raman spectrometer (New Mills, UK). Analyses were conducted at room temperature with a 514 nm laser equipped with an Olympus microscope and a CCD detector.

The morphology of the synthesized oxides was analyzed via scanning electron microscopy (SEM) with a GeminiSEM 500 from Zeiss (Oberkochen, Germany) and transmission electron microscopy (TEM) with a JEM 2100F (JEOL Ltd., Tokyo, Japan) 200 kV

field emission microscope equipped with a Gatan OneView camera. Energy dispersive X-ray spectroscopy elemental point scan analyses were conducted on a EDS X-Max 80 de Oxford Instruments (High Wycombe, UK), with a 127 eV resolution. Nanoparticle size and distribution were obtained through image analyses using ImageJ software (Version 1.53j, NIH, USA) [42].

4.3. Dry Reforming of Methane Reaction Tests

Dry reforming of methane was carried out in a fixed-bed reactor setup. The reactor consisted of a quartz tube of a $\frac{1}{2}$ inch inner diameter placed inside a tubular vertical electrical furnace. The oxide samples (0.25 g) were placed over a quartz frit located at half of the quartz tube (total length 41 cm). Temperature was controlled with a K-type thermocouple in contact with the oxide bed and covered by a quartz shield. For the reaction tests, the materials were pressed into pellets, crushed, and sieved in 200–400 μm sieves. In a typical experiment, the temperature was raised to 850 °C under an Ar (Praxair) atmosphere (100 mL min^{-1}). Then, CH_4 and CO_2 were injected with a total flow of 100 mL min^{-1} , with a volume fraction $\text{CH}_4:\text{CO}_2:\text{Ar}$ ratio of 5:5:90 and a hourly space velocity of 24 L $\text{g}^{-1} \text{h}^{-1}$. The gas bottles were of 10% CH_4 balanced in Ar and 15% CO_2 balanced in Ar. Gas outlet was analyzed by using a Micro-GC CP-4900 (Varian, Santa Clara, CA, USA) gas chromatograph equipped with Molsieve5A and PoraPlot-Q glass capillary modules. CH_4 (X_{CH_4}) and CO_2 (X_{CO_2}) conversion and CO (S_{CO}) and H_2 (S_{H_2}) selectivity were determined according to the following equations:

$$X_{\text{CH}_4} = \frac{n_{\text{CH}_4, \text{in}} - n_{\text{CH}_4, \text{out}}}{n_{\text{CH}_4, \text{in}}} \cdot 100 \quad (3)$$

$$X_{\text{CO}_2} = \frac{n_{\text{CO}_2, \text{in}} - n_{\text{CO}_2, \text{out}}}{n_{\text{CO}_2, \text{in}}} \cdot 100 \quad (4)$$

$$S_{\text{CO}} = \frac{n_{\text{CO}}}{\left(n_{\text{CO}_2, \text{in}} - n_{\text{CO}_2, \text{out}}\right) + \left(n_{\text{CH}_4, \text{in}} - n_{\text{CH}_4, \text{out}}\right)} \cdot 100 \quad (5)$$

$$S_{\text{H}_2} = \frac{n_{\text{H}_2}}{2 \cdot \left(n_{\text{CH}_4, \text{in}} - n_{\text{CH}_4, \text{out}}\right)} \cdot 100 \quad (6)$$

Supplementary Materials: The following are available online at <https://www.mdpi.com/article/10.3390/catal11060741/s1>, Figure S1: Rietveld refinement exemplified for $\text{Sr}_2\text{Fe}_{0.5}\text{Ni}_{0.5}\text{MoO}_{6-\delta}$ material as synthesized (calcination at 1100 °C in air). Due to Ni doping on B-site there is a shift from the observed data to the reference taken for the double perovskite, $\text{Sr}_2\text{FeMoO}_6$, Figure: S2. CO (S_{CO}) and H_2 selectivity (S_{H_2}) for the four materials, measured at 10 h on stream. (T = 850 °C).

Author Contributions: Conceptualization, A.J.C. and J.M.S.; Methodology, A.J.C.; Investigation, A.J.C.; Resources, A.J.C. and J.M.S.; Data Curation, A.J.C.; Writing—Original Draft Preparation, A.J.C.; Writing—Review & Editing, J.M.S.; Supervision, J.M.S.; Project Administration, A.J.C. and J.M.S.; Funding Acquisition, A.J.C. and J.M.S. All authors have read and agreed to the published version of the manuscript.

Funding: The project that gave rise to these results received the support of a fellowship from “la Caixa” Foundation (ID 100010434). The fellowship code is LCF/BQ/PI20/11760015. Additional funding from the Spanish Government (Grant RTI2018-102161) is also acknowledged.

Acknowledgments: A.J.C. is grateful for the help of José Luis Jordá in performing the in situ XRD analysis; Alejandro Gamir with the Rietveld refinements; and Andrés López for performing the XRD analyses after the reaction. We thank the support of the Electronic Microscopy Service of the Universitat Politècnica de València.

Conflicts of Interest: The authors declare no conflict of interest.

References

1. Munnik, P.; De Jongh, P.E.; De Jong, K.P. Recent Developments in the Synthesis of Supported Catalysts. *Chem. Rev.* **2015**, *115*, 6687–6718. [[CrossRef](#)]
2. Hansen, T.W.; DeLaRiva, A.T.; Challa, S.R.; Datye, A.K. Sintering of Catalytic Nanoparticles: Particle Migration or Ostwald Ripening? *Acc. Chem. Res.* **2013**, *46*, 1720–1730. [[CrossRef](#)]
3. Wang, C.; Wang, Y.; Chen, M.; Liang, D.; Yang, Z.; Cheng, W.; Tang, Z.; Wang, J.; Zhang, H. Recent advances during CH₄ dry reforming for syngas production: A mini review. *Int. J. Hydrogen Energy* **2021**, *46*, 5852–5874. [[CrossRef](#)]
4. Kim, J.H.; Kim, J.K.; Liu, J.; Curcio, A.; Jang, J.; Kim, I.; Ciucci, F.; Jung, W. Nanoparticle Ex-solution for Supported Catalysts: Materials Design, Mechanism and Future Perspectives. *ACS Nano* **2020**. [[CrossRef](#)]
5. Zhang, J.; Gao, M.; Luo, J.-L. In Situ Exsolved Metal Nanoparticles: A Smart Approach for Optimization of Catalysts. *Chem. Mater.* **2020**, *32*, 5424–5441. [[CrossRef](#)]
6. Kousi, K.; Tang, C.; Metcalfe, I.S.; Neagu, D. Emergence and Future of Exsolved Materials. *Small* **2021**, 2006479. [[CrossRef](#)]
7. Neagu, D.; Oh, T.S.; Miller, D.N.; Menard, H.; Bukhari, S.M.; Gamble, S.R.; Gorte, R.J.; Vohs, J.M.; Irvine, J.T. Nano-socketed nickel particles with enhanced coking resistance grown in situ by redox exsolution. *Nat. Commun.* **2015**, *6*, 8120. [[CrossRef](#)] [[PubMed](#)]
8. Naeem, M.A.; Abdala, P.M.; Armutlulu, A.; Kim, S.M.; Fedorov, A.; Müller, C.R. Exsolution of Metallic Ru Nanoparticles from Defective, Fluorite-Type Solid Solutions Sm₂Ru_xCe_{2-x}O₇ To Impart Stability on Dry Reforming Catalysts. *ACS Catal.* **2020**, *10*, 1923–1937. [[CrossRef](#)]
9. Carrillo, A.J.; Navarrete, L.; Laquiem, M.; Balaguer, M.; Serra, J.M. Boosting methane partial oxidation on ceria through exsolution of robust Ru nanoparticles. *Mater. Adv.* **2021**, *2*, 2924–2934. [[CrossRef](#)]
10. Bhattar, S.; Abedin, M.A.; Kanitkar, S.; Spivey, J.J. A review on dry reforming of methane over perovskite derived catalysts. *Catal. Today* **2020**. [[CrossRef](#)]
11. Sun, X.; Chen, H.; Yin, Y.; Curnan, M.T.; Han, J.W.; Chen, Y.; Ma, Z. Progress of Exsolved Metal Nanoparticles on Oxides as High Performance (Electro)Catalysts for the Conversion of Small Molecules. *Small* **2021**, 2005383. [[CrossRef](#)] [[PubMed](#)]
12. Otto, S.; Kousi, K.; Neagu, D.; Bekris, L.; Janek, J.; Metcalfe, I.S. Exsolved Nickel Nanoparticles Acting as Oxygen Storage Reservoirs and Active Sites for Redox CH₄ Conversion. *ACS Appl. Energy Mater.* **2019**, *2*, 7288–7298. [[CrossRef](#)]
13. Kousi, K.; Neagu, D.; Bekris, L.; Cali, E.; Kerherve, G.; Papaioannou, E.I.; Payne, D.J.; Metcalfe, I.S. Low temperature methane conversion with perovskite-supported exo/endo -particles. *J. Mater. Chem. A* **2020**, *8*, 12406–12417. [[CrossRef](#)]
14. Kousi, K.; Neagu, D.; Bekris, L.; Papaioannou, E.I.; Metcalfe, I.S. Endogenous Nanoparticles Strain Perovskite Host Lattice Providing Oxygen Capacity and Driving Oxygen Exchange and CH₄ Conversion to Syngas. *Angew. Chem. Int. Ed.* **2020**, *59*, 2510–2519. [[CrossRef](#)] [[PubMed](#)]
15. Carrillo, A.J.; Kim, K.J.; Hood, Z.D.; Bork, A.H.; Rupp, J.L.M. La_{0.6}Sr_{0.4}Cr_{0.8}Co_{0.2}O₃ Perovskite Decorated with Exsolved Co Nanoparticles for Stable CO₂ Splitting and Syngas Production. *ACS Appl. Energy Mater.* **2020**, *3*, 4569–4579. [[CrossRef](#)]
16. Zubenko, D.; Singh, S.; Rosen, B.A. Exsolution of Re-alloy catalysts with enhanced stability for methane dry reforming. *Appl. Catal. B Environ.* **2017**, *209*, 711–719. [[CrossRef](#)]
17. Papargyriou, D.; Miller, D.N.; Sirt Irvine, J.T. Exsolution of Fe–Ni alloy nanoparticles from (La,Sr)(Cr,Fe,Ni)O₃ perovskites as potential oxygen transport membrane catalysts for methane reforming. *J. Mater. Chem. A* **2019**, *7*, 15812–15822. [[CrossRef](#)]
18. Joo, S.; Kwon, O.; Kim, K.; Kim, S.; Kim, H.; Shin, J.; Jeong, H.Y.; Sengodan, S.; Han, J.W.; Kim, G. Cation-swapped homogeneous nanoparticles in perovskite oxides for high power density. *Nat. Commun.* **2019**, *10*, 1–9. [[CrossRef](#)]
19. Kwon, O.; Kim, K.; Joo, S.; Jeong, H.Y.; Shin, J.; Han, J.W.; Sengodan, S.; Kim, G. Self-assembled alloy nanoparticles in a layered double perovskite as a fuel oxidation catalyst for solid oxide fuel cells. *J. Mater. Chem. A* **2018**, *6*, 15947–15953. [[CrossRef](#)]
20. Wang, H.; Dong, X.; Zhao, T.; Yu, H.; Li, M. Dry reforming of methane over bimetallic Ni–Co catalyst prepared from La(Co_xNi_{1-x})_{0.5}Fe_{0.5}O₃ perovskite precursor: Catalytic activity and coking resistance. *Appl. Catal. B Environ.* **2019**, *245*, 302–313. [[CrossRef](#)]
21. Tsoukalou, A.; Imtiaz, Q.; Kim, S.M.; Abdala, P.M.; Yoon, S.; Müller, C.R. Dry-reforming of methane over bimetallic Ni–M/La₂O₃ (M=Co, Fe): The effect of the rate of La₂O₂CO₃ formation and phase stability on the catalytic activity and stability. *J. Catal.* **2016**, *343*, 208–214. [[CrossRef](#)]
22. Du, Z.; Zhao, H.; Yi, S.; Xia, Q.; Gong, Y.; Zhang, Y.; Cheng, X.; Li, Y.; Gu, L.; Świerczek, K. High-Performance Anode Material Sr₂FeMo_{0.65}Ni_{0.35}O_{6-δ} with In Situ Exsolved Nanoparticle Catalyst. *ACS Nano* **2016**, *10*, 8660–8669. [[CrossRef](#)] [[PubMed](#)]
23. Wang, Y.; Liu, T.; Li, M.; Xia, C.; Zhou, B.; Chen, F. Exsolved Fe–Ni nano-particles from Sr₂Fe_{1.3}Ni_{0.2}Mo_{0.5}O₆ perovskite oxide as a cathode for solid oxide steam electrolysis cells. *J. Mater. Chem. A* **2016**, *4*, 14163–14169. [[CrossRef](#)]
24. Li, J.; Yu, Y.; Yin, Y.M.; Zhou, N.; Ma, Z.F. A novel high performance composite anode with in situ growth of Fe–Ni alloy nanoparticles for intermediate solid oxide fuel cells. *Electrochim. Acta* **2017**, *235*, 317–322. [[CrossRef](#)]
25. Zhu, T.; Troiani, H.E.; Moggi, L.V.; Han, M.; Barnett, S.A. Ni-Substituted Sr(Ti,Fe)O₃ SOFC Anodes: Achieving High Performance via Metal Alloy Nanoparticle Exsolution. *Joule* **2018**, *2*, 478–496. [[CrossRef](#)]
26. Chang, H.; Chen, H.; Yang, G.; Shi, J.; Zhou, W.; Bai, J.; Wang, Y.; Li, S.D. Enhanced coking resistance of Ni cermet anodes for solid oxide fuel cells based on methane on-cell reforming by a redox-stable double-perovskite Sr₂MoFeO_{6-δ}. *Int. J. Energy Res.* **2019**, *43*, 2527–2537. [[CrossRef](#)]
27. Jiang, Y.; Yang, Y.; Xia, C.; Bouwmeester, H.J.M. Sr₂Fe_{1.4}Mn_{0.1}Mo_{0.5}O_{6-δ} perovskite cathode for highly efficient CO₂ electrolysis. *J. Mater. Chem. A* **2019**, *7*, 22939–22949. [[CrossRef](#)]

28. Lv, H.; Lin, L.; Zhang, X.; Song, Y.; Matsumoto, H.; Zeng, C.; Ta, N.; Liu, W.; Gao, D.; Wang, G.; et al. In Situ Investigation of Reversible Exsolution/Dissolution of CoFe Alloy Nanoparticles in a Co-Doped $\text{Sr}_2\text{Fe}_{1.5}\text{Mo}_{0.5}\text{O}_{6-\delta}$ Cathode for CO_2 Electrolysis. *Adv. Mater.* **2020**, *32*, 1906193. [[CrossRef](#)] [[PubMed](#)]
29. Chen, L.; Xu, J.; Wang, X.; Xie, K. $\text{Sr}_2\text{Fe}_{1.5+x}\text{Mo}_{0.5}\text{O}_{6-\delta}$ cathode with exsolved Fe nanoparticles for enhanced CO_2 electrolysis. *Int. J. Hydrogen Energy* **2020**, *45*, 11901–11907. [[CrossRef](#)]
30. Meng, X.; Wang, Y.; Zhao, Y.; Zhang, T.; Yu, N.; Chen, X.; Miao, M.; Liu, T. In-situ exsolution of nanoparticles from Ni substituted $\text{Sr}_2\text{Fe}_{1.5}\text{Mo}_{0.5}\text{O}_6$ perovskite oxides with different Ni doping contents. *Electrochim. Acta* **2020**, *348*, 136351. [[CrossRef](#)]
31. Zhu, K.; Wu, T.; Li, M.; Lu, R.; Zhu, X.; Yang, W. Perovskites decorated with oxygen vacancies and Fe-Ni alloy nanoparticles as high-efficiency electrocatalysts for the oxygen evolution reaction. *J. Mater. Chem. A* **2017**, *5*, 19836–19845. [[CrossRef](#)]
32. Lv, H.; Lin, L.; Zhang, X.; Gao, D.; Song, Y.; Zhou, Y.; Liu, Q.; Wang, G.; Bao, X. In situ exsolved FeNi_3 nanoparticles on nickel doped $\text{Sr}_2\text{Fe}_{1.5}\text{Mo}_{0.5}\text{O}_{6-\delta}$ perovskite for efficient electrochemical CO_2 reduction reaction. *J. Mater. Chem. A* **2019**, *7*, 11967–11975. [[CrossRef](#)]
33. Sun, Y.F.; Li, J.H.; Cui, L.; Hua, B.; Cui, S.H.; Li, J.H.; Luo, J.L. A-site-deficiency facilitated in situ growth of bimetallic Ni-Fe nano-alloys: A novel coking-tolerant fuel cell anode catalyst. *Nanoscale* **2015**, *7*, 11173–11181. [[CrossRef](#)] [[PubMed](#)]
34. Spring, J.; Sediva, E.; Hood, Z.D.; Gonzalez-Rosillo, J.C.; O’Leary, W.; Kim, K.J.; Carrillo, A.J.; Rupp, J.L.M. Toward Controlling Filament Size and Location for Resistive Switches via Nanoparticle Exsolution at Oxide Interfaces. *Small* **2020**, *16*, 2003224. [[CrossRef](#)] [[PubMed](#)]
35. Gao, Y.; Chen, D.; Saccoccio, M.; Lu, Z.; Ciucci, F. From Material Design to Mechanism study: Nanoscale Ni Exsolution on a Highly Active A-site Deficient Anode Material for Solid Oxide Fuel Cells. *Nano Energy* **2016**, *27*, 499–508. [[CrossRef](#)]
36. Tang, C.; Kousi, K.; Neagu, D.; Portolés, J.; Papaioannou, E.I.; Metcalfe, I.S. Towards efficient use of noble metals via exsolution exemplified for CO oxidation. *Nanoscale* **2019**, *11*, 16935–16944. [[CrossRef](#)]
37. Momma, K.; Izumi, F. VESTA 3 for three-dimensional visualization of crystal, volumetric and morphology data. *J. Appl. Crystallogr.* **2011**, *44*, 1272–1276. [[CrossRef](#)]
38. Vecino-Mantilla, S.; Gauthier-Maradei, P.; Huvé, M.; Serra, J.M.; Roussel, P.; Gauthier, G.H. Nickel Exsolution-Driven Phase Transformation from an $n = 2$ to an $n = 1$ Ruddlesden-Popper Manganite for Methane Steam Reforming Reaction in SOFC Conditions. *ChemCatChem* **2019**, *11*, 4631–4641. [[CrossRef](#)]
39. Gálvez, M.E.; Jacot, R.; Scheffe, J.; Cooper, T.; Patzke, G.; Steinfeld, A. Physico-chemical changes in Ca, Sr and Al-doped La-Mn-O perovskites upon thermochemical splitting of CO_2 via redox cycling. *Phys. Chem. Chem. Phys.* **2015**, *17*, 6629–6634. [[CrossRef](#)]
40. Ezbiri, M.; Takacs, M.; Stolz, B.; Lungthok, J.; Steinfeld, A.; Michalsky, R. Design principles of perovskites for solar-driven thermochemical splitting of CO_2 . *J. Mater. Chem. A* **2017**, *5*, 15105–15115. [[CrossRef](#)]
41. Donat, F.; Müller, C.R. CO_2 -free conversion of CH_4 to syngas using chemical looping. *Appl. Catal. B Environ.* **2020**, *278*, 119328. [[CrossRef](#)]
42. Schneider, C.A.; Rasband, W.S.; Eliceiri, K.W. NIH Image to ImageJ: 25 years of image analysis. *Nat. Methods* **2012**, *9*, 671–675. [[CrossRef](#)] [[PubMed](#)]